Operando X-ray Absorption Spectroscopic Study of Ultradispersed Mo/TiO 2 CO 2 -Hydrogenation Catalysts: Why Does Rutile Promote Methanol Synthesis?

T. Len, P. Afanasiev, Y. Yan, M. Aouine, F. Morfin, L. Piccolo

Operando X-ray absorption spectroscopic study of ultradispersed Mo/TiO_2 CO_2-hydrogenation catalysts: why does rutile promote methanol synthesis?

T. Len, P. Afanasiev,* Y. Yan, M. Aouine, F. Morfin, L. Piccolo*

IRCELYON, CNRS & Université Lyon 1, F-69626 Villeurbanne, France

** Corresponding authors. E-mails: pavel.afanasiev@ircelyon.univ-lyon1.fr; laurent.piccolo@ircelyon.univ-lyon1.fr*

Abstract

CO_2 hydrogenation to methanol is an important process for an ecologic and energetic shift, which stimulates the development of active catalysts based on non-critical elements. We have recently reported that Mo atoms anchored on rutile titania nanorods exhibit distinctive performance in methanol synthesis, i.e. higher activity and methanol selectivity than Mo dispersed on anatase and P25 commercial forms. In this work, for deciphering the origin of the higher performance of rutile, this support is compared to other selected oxides of interest, and Mo/TiO_2 catalysts are investigated *operando* at high pressure by synchrotron X-ray absorption spectroscopy at the Mo K edge combined with chemometric treatments. The main structural change occurs during the reductive activation pretreatment, when Mo^{VI} species convert to more reduced ones. However, while on anatase titania the active species are mostly MoO_2-like clusters, on rutile titania single Mo atoms are not only more present but may also replace surface Ti atoms, which would explain the more stable single-atomic dispersion and the rutile-like coordination of Mo, as well as the low sensitivity of the latter to the chemical environment and the metal loading. As a result, Mo-doped rutile titania acts as a promising atomically dispersed catalyst for CO_2 hydrogenation to methanol.

Keywords

Metal ultradispersion, single-atom catalysis, molybdenum on titania, CO_2 hydrogenation, methanol synthesis, operando XAS

Introduction

In the context of global warming and related carbon capture & utilization strategies, the thermocatalytic hydrogenation of CO_2 is one possible route toward the production of "green" fuels and platform chemicals.[1] As far as methanol production is concerned, besides the industrial $Cu/ZnO/Al_2O_3$ syngas-to-methanol catalyst which is vulnerable to water produced during CO_2 hydrogenation,[2] a number of materials have been proposed to increase the methanol yields and catalyst stability, but they mostly involve rare or strategic elements[3,4] such as Au, Pd, Pt, In, Ga, and Zn.[5–8]

From these previous works, one can conclude on two main structural aspects that characterize good CO_2-to-methanol catalysts, which can be interrelated: i) presence of metal/oxide or oxide/oxide interface with adequate interaction, and/or ii) oxide reducibility and presence of oxygen vacancies. Note that "oxide" can be replaced with "sulfide" or "carbide", especially when dealing with Mo compounds.[9,10] With the recent development of single-atom catalysis,[11–14] and in line with the importance of metal/oxide interfaces and oxygen vacancies, noble metal-doped reducible oxides such as $Pd\text{-}In_2O_3$ were shown to exhibit good performances.[15–18] In addition, molybdenum and titanium oxides appeared as interesting partners to late transition metals for promoting the reaction,[19–22] while theoretical calculations predicted that early/mid transition metal atoms anchored on titania may activate CO_2 as well.[23] For a given metal/titania couple, it was also shown that the selectivity to methanol *versus* methane or CO strongly depends on the titania phase through – again – the nature of the metal/oxide interaction.[22,24]

We have recently reported on the catalytic properties of the Mo/TiO_2 system,[25] which was previously regarded as inactive for CO_2 hydrogenation to methanol when not promoted with a strong H_2 activation source such as Pt nanoparticles.[19,26] The performance of this catalyst appeared highly sensitive to the Mo loading (0.1-10 wt%) and the titania type (phase composition, surface area, nanoparticle morphology). In particular, molybdenum supported at intermediate loading (3 wt%) on rutile titania nanorods (RNRs) exhibited unexpected efficiency in terms of total activity, methanol yield, and methanol selectivity. In a first attempt to understand the origin of this performance, we investigated the dispersion, oxidation state and reducibility of molybdenum with scanning transmission electron microscopy (STEM), near-ambient-pressure X-ray photoelectron spectroscopy (NAP-XPS) and temperature-programmed techniques. This work suggested that the RNR support would stabilize atomically dispersed molybdate species with lower Mo oxidation state and enhanced reducibility with respect to other titanias. However, these conclusions were drawn from low-pressure

analyses whereas the reaction is performed at high pressure (2-3 MPa in our case) and molybdenum is highly sensitive to its chemical environment.

In the present article, together with aberration-corrected STEM and *in situ* X-ray diffraction, we use *operando* X-ray absorption spectroscopy to investigate the support-dependent formation and nature of MoO_x species upon catalyst preparation, as well as the evolution of the local coordination environment of molybdenum under reducing treatment and high-pressure reaction conditions. Besides titania, the structure and catalytic performance of molybdenum ultradispersed over other oxides of interest for CO_2-to-methanol reaction, are also disclosed. The most active surface phase is shown to be atomically dispersed Mo anchored at the (110) facets of rutile nanorods.

Experimental

Catalyst preparation

Alumina, titania P25 and DT51D, zinc oxide, zirconia and ceria supports were commercial powders, as reported later on. Rutile nanorods (RNRs) were prepared by hydrothermal synthesis.[27–29] An aqueous solution of ammonia (mixture of 120 mL aqueous NH_3 [25 wt%] and 300 mL water) was added to an aqueous solution of $TiOCl_2$ (mixture of 100 mL $TiOCl_2$ [15 wt% Ti] and 100 mL water) up to reaching a pH of zero. The resulting solution, which contains rutile nuclei, was stirred overnight, added with H_2SO_4 (10 g of concentrated sulfuric acid for 80 mL of solution) and heated at 200 °C in a Teflon autoclave for 48 h. After centrifugation and filtration, the titania powder was washed with demineralized water until pH 7, and finally dried at 60 °C overnight in air. The RNRs are 50-100 nm-long, present a square cross section of side 10-20 nm, and exhibit mostly (110) facets.

3Mo/oxide catalysts were prepared by wet impregnation. In a typical synthesis, 5 g of support was added to a 60 mL solution of demineralized water containing 300 mg of ammonium heptamolybdate (AHM), $(NH_4)_6Mo_7O_{24}.4H_2O$ (Sigma-Aldrich, 99.98%). After 2 h of magnetic stirring, the solvent was removed using a rotating evaporator. The impregnate was then recovered and reduced in order to decompose the precursor. For the reduction, the powder was placed in a quartz tubular U-shaped reactor with an internal diameter of 10 mm. The reactor was placed in a tubular furnace and H_2 was flowed through the powder at a flow rate of 40 mL/min after purging with N_2. The reactor was then heated up to 500 °C with a ramp of 5°C/min, followed by a plateau of 2 h.

Catalytic testing

The catalytic CO_2 hydrogenation tests were conducted using a straight stainless-steel flow fixed bed reactor with an internal diameter of 7 mm, heated by a tubular oven. Gas flows were controlled by Brooks Instruments flowmeters and analyzed, after depressurization to atmospheric pressure, with an Inficon Fusion micro gas chromatograph equipped with RT-Q-Bond and molecular sieve columns. The reactor total pressure was set to 3 MPa using a Tescom ER5000 electro-pneumatic PID controller driving a Tescom membrane backpressure regulator. A heating system was set up to keep the temperature above 70 °C in the gas lines to avoid water condensation. Prior to catalytic tests, the as-prepared catalysts were treated *in situ* in the catalytic reactor under H_2 (40 mL/min) for 2 h at atmospheric pressure and 450 °C (5 °C/min).

The catalytic tests were conducted with an $H_2/CO_2/N_2$ mixture (3:1:1 vol. fractions and 50 mL/min total molar flow rate) and 400 mg of catalyst, leading to a space velocity of 7500 $mL.g^{-1}.h^{-1}$. After pressurization of the reactor near room temperature (RT) with the reactive mixture, the following standard temperature sequence was used for the catalytic tests: from RT to 200 °C at 5 °C/min, then 200 °C to 300 °C at 0.25 °C/min.

The conversion of CO_2 (χ_{CO2}), selectivity to product P (S_P), yield of product P (Y_P) and methanol space-time yield (STY_{MeOH}) were calculated using equations (1) to (4), respectively. Q_{CO2}^{in}, Q_i^{out}, $M_{MeOH,}$ and m_{cat} represent the molar flow rate of CO_2 at the reactor inlet, the molar flow rate of carbon atoms contained in the flow of product *i* at the reactor outlet, the molar mass of methanol, and the catalyst mass, respectively.

$$\chi_{CO2} = \frac{\sum_i Q_i^{out}}{Q_{CO2}^{in}} \quad (1)$$

$$S_P = \frac{Q_P^{out}}{\sum_i Q_i^{out}} \quad (2)$$

$$Y_P = \chi_{CO2} S_P = \frac{Q_P^{out}}{Q_{CO2}^{in}} \quad (3)$$

$$STY_{MeOH} = \frac{Q_{CO2}^{in}\, \chi_{CO2}\, S_{MeOH}\, M_{MeOH}}{m_{cat}} \quad (4)$$

Laboratory characterization

Scanning transmission electron microscopy (STEM) with high-angle annular dark field (HAADF) detection was performed on a Jeol Cold FEG NeoARM equipped with a Cs-corrected condenser at the probe level and operated at 200 kV and a FEI Titan ETEM G2 equipped with a Cs-corrector of the

objective lens and operated at 300 kV. For sample preparation, the powder was crushed and dispersed in ethanol through ultrasonication, dropped onto a holey carbon-coated 200 mesh Cu grid, and dried by a lamp. To avoid contamination during analysis and remove any residual carbon, the samples were Ar plasma-cleaned for 20 s (Plasma Prep 5, GaLa Instrumente). No filtering was applied on the STEM images.

Powder X-ray diffraction (XRD) was performed using a Bruker D8 Advance and Cu Kα radiation. *In situ* XRD was performed using an H_2 flow rate of 25 mL/min in an Anton Paar XRK900 Z-motorized reaction chamber. The temperature program was composed of ramps (2 °C/min) and plateaus at selected temperatures for stabilization (15 min) and recording of the diffractograms (*ca*. 120 min, *ca*. 26 h overall), which were acquired from 20° to 80° (2θ) by step of 0.02 °. The lattice parameters and the crystallite sizes were obtained from Rietvield analysis of the diffractograms.

X-ray fluorescence (XRF) analysis was performed using an Epsilon 4 spectrometer from Malvern Panalytical. The generator was used at 50 kV and 60 µA under air atmosphere. Data were collected at the Mo Kα energy level (17.44 keV) using a 3-point calibration curve verified by inductively coupled plasma – optical emission spectroscopy (ICP-OES, Horiba Jobin Yvon Activa).

The specific surface areas were determined, after a desorption step at 250 °C for 3 h under vacuum, by N_2 volumetry through a 5-points BET method using a Micrometrics ASAP 2020 device.

Synchrotron X-ray absorption spectroscopy

The X-ray absorption spectroscopy (XAS) experiments were performed in the transmission mode at the Mo K edge on the ROCK beamline of the SOLEIL synchrotron.[30] The spectra were recorded using a Si(220) channel-cut monochromator. The monochromator rocking frequency was 500 ms per spectrum. A bulk Mo foil was used as a reference simultaneously measured with all our samples, to align the spectra. The edge position of the Mo foil at absorbance 0.5 was set to 20 000 eV. The samples were placed in quartz capillaries (internal diameter 1.2 mm, wall thickness 20 µm) through a 4 mm-long catalyst bed, closed with quartz wool, and connected to a gas distribution system. A thermocouple probed the quartz wool zone at the inlet of the capillaries. The capillaries were heated up to 800 °C with a calibrated air blower. The effluent gases were continuously monitored with a mass spectrometer.

The following acquisition conditions were used for *in situ* experiments on Mo/oxide catalysts: i) He flow (30 mL/min) at 1 atm and RT; ii) switch to H_2 flow (30 mL/min) at 1 atm and heating to 450 °C (10 °C/min); iii) cooling down to 100 °C in H_2 flow; iv) switch to H_2+CO_2 flow (3:1, total flow rate 30 mL/min)

and pressurization to 2 MPa with heating (5 °C/min) to 225 °C (~40 min plateau), 275 °C (~10 min plateau) and 350 °C (~10 min plateau); v) switch to H_2 only, depressurization to 1 atm and cooling to ~60 °C, then switch to He flow. For *in situ* experiments on AHM/TiO_2 impregnates, the samples were heated in H_2 flow (30 mL/min) at 1 atm from RT to *ca.* 800 °C (10 °C/min).

Data merging and preliminary analysis were carried out using ATHENA software.[31] The scattering paths were calculated using FEFF6 software.[31] The input files were generated from the Materials Project's CIF files mp-20589 of MoO_3 (for Mo=O, Mo-O, and non-bonded Mo-O-Mo) and mp-510536 of MoO_2 (for the "metallic" Mo-Mo shell).

EXAFS fitting was performed using the VIPER program,[32] alternatively in *k* and *R* spaces. When in the *R* space, it was done in the (Im + Module) mode. During the fitting procedure the values of *R* (radial distance), *CN* (coordination number), σ^2 (distance variance) and ΔE_0 (energy difference) were varied. The goodness of the fit was determined by the value of the R-factor. The S_0^2 value of 0.85 ± 0.05 was obtained from a Na_2MoO_4 reference spectrum using the decorrelation procedure at variable *k* weights, as described previously.[33] The *k* and *R* ranges used for EXAFS fitting were slightly varied as a function of the spectrum shape and the level of noise. The *k*-range was from 3 to 14 or 15 $Å^{-1}$, while the *R*-range was from 1 Å to the end of the meaningful part of the Fourier transform (FT) spectrum (3.5-4.0 Å). As the starting structural information was lacking and the presence of mixtures of different (disordered) species was highly probable, we followed the "shell-by-shell fitting protocol": we began with a minimal set of shells corresponding to the number of visible FT peaks, then we extended it on-the-fly as long as it appeared necessary.

Continuous Cauchy wavelet transform (CCWT) was applied for the qualitative analysis of EXAFS spectra, using a MATLAB script by Muñoz *et al*.[34] The EXAFS signals were visualized in three dimensions: the wavevector (*k*), the interatomic distance uncorrected for phase-shifts (*R*), and the CCWT modulus. The CCWT maps provide straightforward qualitative visual information related to the *k*-range of each "*R*-EXAFS" contribution, which is useful to identify the nearest neighbors.[34]

To analyze intermediate species appearing during the pretreatment and the reaction, we applied a set of data analysis tools, as described in Ref. 35. First, we constructed a matrix of the raw data composed of normalized spectra recorded during a specific process, using a homemade XAS-SVD MATLAB toolbox. Then, preliminary principal component analysis (PCA) was performed to estimate the number of components, from the scree plot of eigenvalues. Afterwards, multivariate curve resolution – alternating least square (MCR-ALS) analysis was applied on the matrix obtained in XAS-SVD to extract pure components and their concentrations.[36] The MCR-ALS analysis of XAS spectra was carried out in the range from 19900 to 20860 eV (*i.e*. up to *k*=15 $Å^{-1}$).

For Mo/rutile, XANES spectra were simulated using the FDMNES program.[37] To build models for simulations, the bulk-substituted structures were generated by replacing Ti^{IV} atoms with one or two Mo^{IV} atoms in a 2×1×1 supercell of rutile, optionally followed by the removal of oxygen atoms from the Mo coordination shell (reduced Mo^{III} and Mo^{II} model superstructures). Surface substitution models were generated by cleaving the rutile structure along the (110) plane and creating a 10 Å vacuum layer above the surface. Then, the same substitution procedure as for the bulk models was carried out in a 2×1 supercell. Optionally, an oxygen atom was attached to the surface Mo atoms, creating a surface molybdenyl Mo^{VI} moiety, to check the effect of surface oxidation. In addition, the surface Ti atoms were optionally hydroxylated in order to assess the model stability and its dependence on the details of the support surface structure. The surface-grafted model structures were created by adsorbing molybdenum oxo-clusters onto the (110) surface of rutile. The clusters correspond to Mo^{VI}, Mo^{IV}, and Mo^{II} species. The XANES spectra were simulated using finite differences and self-consistent field (SCF). The convolution was carried out using default tabulated values of core-hole width. A reasonable level of convergence *vs.* the calculation cluster radius was achieved at R = 6 Å.

Results

Comparison between Mo catalysts supported on various oxides

Molybdenum was impregnated with 3-10 wt% Mo loading onto seven different metal oxide supports, including three TiO_2 types (commercial DT51D anatase, commercial P25 anatase-rutile mixture, and homemade rutile nanorods), as summarized in Table 1. The catalysts are referred to as <*loading in wt%*>Mo/<*oxide*>.

Table 1. Main characteristics of oxide powder supports and Mo/oxide samples.

Sample name	Furnisher, commercial name (purity)	Specific surface area (m^2/g)	Phase [c]	Mo loading (wt%)
Al_2O_3	Sasol, Puralox SCFa-140 (97%)	157[a]	Cubic (γ)	–
3Mo/Al_2O_3	–	158[b]		3.1[d]
TiO_2-DT51D	Tronox, CristalActiv DT51D (99%)	85[a]	Anatase	–
3Mo/TiO_2-DT51D	–	78[b]		2.9[e]
10Mo/TiO_2-DT51D	–	ND		8.3[e]
TiO_2-P25	Evonik, Aeroxide P25 (99.5%)	65[a]	80% anatase	–
3Mo/TiO_2-P25	–	61[b]	20% rutile	2.8[e]
10Mo/TiO_2-P25	–	ND		8.2[e]
TiO_2-RNR	–	44[b]		–
3Mo/TiO_2-RNR	–	44[b]	Rutile	2.9[e]
10Mo/TiO_2-RNR	–	ND		11.2[e]
ZnO	Alfa Aesar, NanoArc (99%)	16[a]	Wurtzite	–
3Mo/ZnO	–	16[b]		3.1[d]/2.9[e]
ZrO_2	Saint-Gobain Norpro, ZirPro 235	216[b]	68% tetragonal 32% monoclinic	–
3Mo/ZrO_2	–	183[b]		3.2[d]
CeO_2	Rhodia, HSA10	123[b]	Fluorite	–
3Mo/CeO_2	–	112[b]		3.0[e]

[a] Supplier values. [b] Determined from N_2 volumetry through BET method. [c] Determined from XRD of the Mo/oxide catalysts. [d] Determined from ICP-OES. [e] Determined from XRF spectroscopy (standard deviation 0.05 wt%). ND: not determined.

Figure S1 shows the X-ray diffractograms of 3Mo/oxide catalysts. No signature of molybdenum is present, suggesting in all cases a high dispersion of the MoO_x phase over the support surface.

Figure 1 and Figures S2-S7 show representative STEM-HAADF images of the Mo/TiO_2 samples (Figure 1a insert and Figures S5-S6 show representative STEM images of the RNRs). Overall, Mo is highly dispersed at the surface of the oxides: at a loading of 3 wt%, Mo is present as both single atoms and clusters, the latter increasing in proportion at 10 wt% Mo, as reported for TiO_2-DT51D in our previous

work.[25] Molybdenum is similarly dispersed on alumina (Figure S8). The other oxide supports were too dense to enable discrimination of Mo atoms from their lattice by STEM.

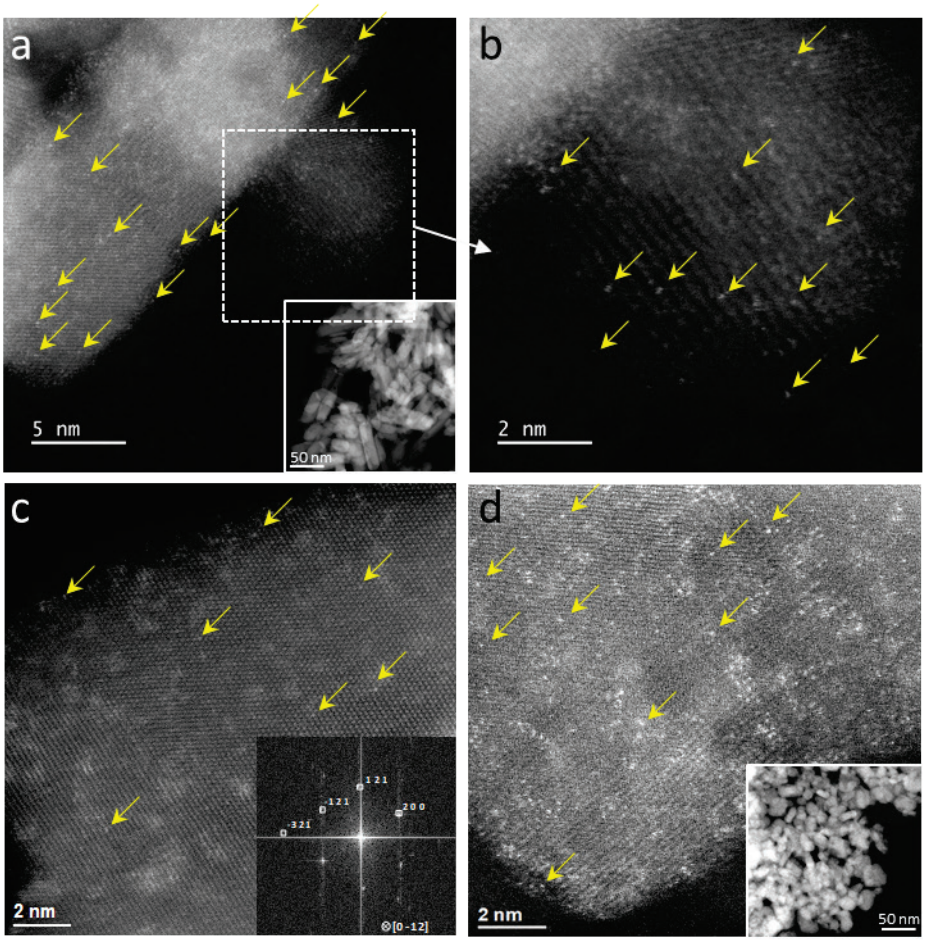

Figure 1. Representative STEM-HAADF images of 3Mo/RNR (a, b) and 3Mo/DT51D (c, d) samples. Arrows point to individual Mo atoms. The inserts in (a) and (d) show low-magnification images of the corresponding samples. The insert in (c) shows a FFT of the image, with assignement of the spots.

To complement STEM and XRD analyses, *ex situ* X-ray absorption spectroscopy experiments were conducted at the molybdenum K-edge. The corresponding spectra together with several relevant references are compiled in Figure 2. While a pre-edge jump is clearly visible for five of the materials, which show similar features as AHM and MoO_3 references, it is less marked for Mo/ZnO and Mo/RNR, which more resemble MoO_2. For the Mo K edge, the pre-edge feature is mostly related to the excitation of a 1s electron to the 4d orbital. This dipole forbidden transition becomes quadrupole allowed due to the non-centrosymmetric coordination of Mo atoms. Moreover, the intensity of this transition increases as the 4d states become emptier, i. e. when the oxidation state of molybdenum increases.[38]

Molybdenum oxide reduction leads to a harder 1s – 4d electronic transition due to a more symmetrical configuration (elongated octahedron) and to the filling of 4d states, which both conduct to the disappearance of the pre-edge. Thus, from this first analysis in ambient air at RT, Mo appears less oxidized on ZnO and TiO_2-RNR than on the other oxides.

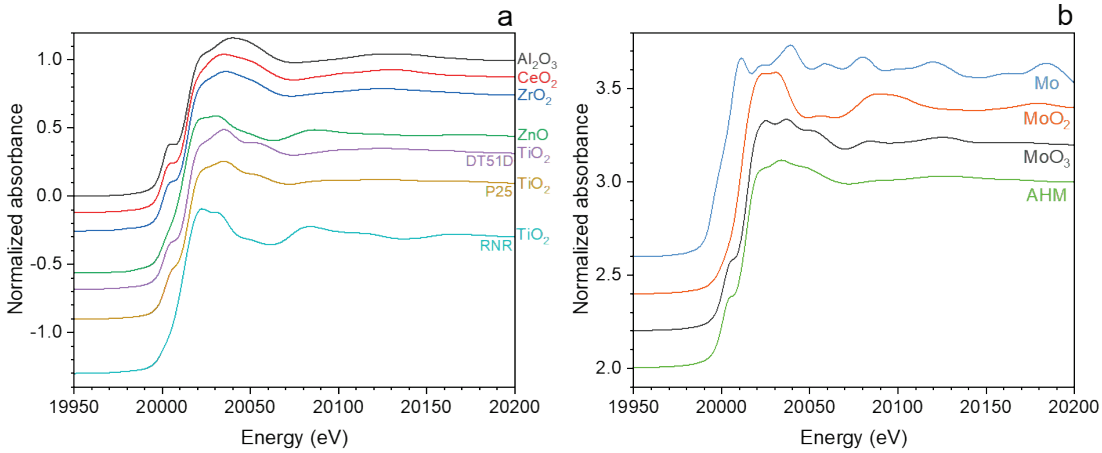

Figure 2. X-ray absorption spectra at the Mo K edge of as-prepared 3 wt% Mo/metal-oxide samples (a) and Mo-containing references (b) recorded in ambient air at RT. AHM stands for ammonium heptamolybdate.

EXAFS analysis was first performed on the 3Mo/oxide as-prepared solids and the references in ambient air conditions ("*ex situ*"), as reported in Figures S9-S12. The structural parameters obtained from numerical fitting are synthesized in Table S1. From these data, consistently with STEM analyses for Mo/TiO_2 and Mo/Al_2O_3, it appears that molybdenum is well dispersed on all the supports, with a cumulative Mo – Mo coordination number ranging from 0 to 1.4, versus 7.5 and 7.2 for MoO_3 and MoO_2, respectively. In addition, Mo – Zn and Mo – Ce contributions were detected for the corresponding catalysts, suggesting a strong interaction between molybdenum and the respective (reducible) oxides.

CO_2 hydrogenation activities of the oxide supports ("Sup") and the Mo/support catalysts ("Cat") are reported in Figure 3. Carbon monoxide (classically obtained through the reverse water-gas shift reaction) and water (which is not measured) are always the main products, followed by methane or methanol. In terms of methanol yield, $3Mo/TiO_2$-RNR is by far the most efficient catalyst, with a space-time yield (STY) of 35 g of methanol per kg of catalyst per hour under our conditions. For comparison, a highly metal-loaded (50 wt% Cu) reference $Cu/ZnO/Al_2O_3$ catalyst shows an STY of 141 g_{MeOH} kg_{cat}^{-1} h^{-}

[1] in the same conditions.[25] The other two titania-supported catalysts are much less selective to methanol. Like for titania, on alumina, ceria and zirconia, Mo addition has a strong promoting effect on CO_2 hydrogenation activity. However, the methanol selectively is less than 10% for most of these catalysts except for Mo on CeO_2 and TiO_2-RNR. Finally, Mo/ZnO is the most selective to methanol, but it is poorly active and has similar performances as bare ZnO, which is the only intrinsically active oxide support. Noting that the surface area of commercial ZnO as well as the corresponding 3Mo/ZnO catalyst is very low (16 m^2/g) and their texture is heterogeneous (Figure S13), other nanostructured ZnO forms with higher BET surface areas (52-72 m^2/g) were synthetized through hydrothermal methods (see details in SI). Upon impregnation of Mo and reduction treatment at 450 °C, the surface areas decreased (23-34 m^2/g). Surprisingly, the activity of bare ZnO decreases as the surface area increases, while the promoting effect of Mo increases (Figure S13). However, the methanol yield remains lower than 1% in our conditions. In the following, the investigations have been focused on TiO_2-supported catalysts only.

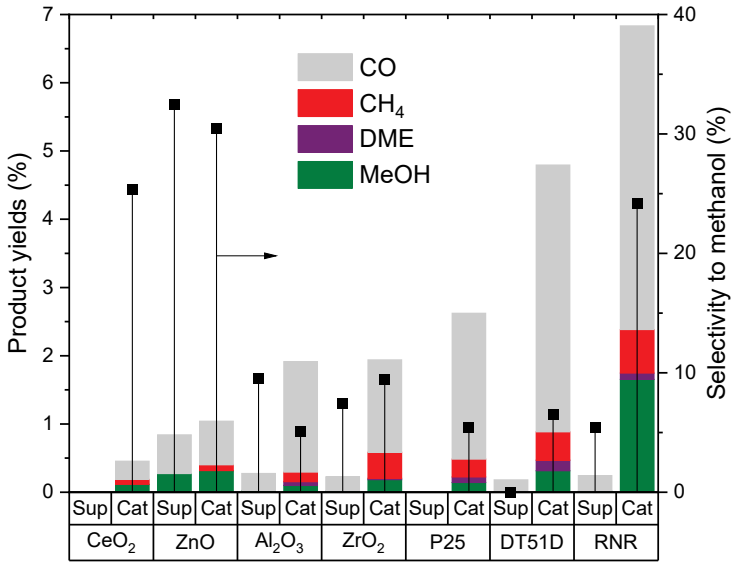

Figure 3. Products yields and methanol selectivity for CO_2 hydrogenation on 3 wt% Mo supported on various oxides ("Cat"). The data are also presented for bare supports ("Sup"). P25, DT51D and RNR relate to TiO_2 types. Reaction conditions: 275 °C, 3 MPa, H_2:CO_2:N_2=3:1:1, Space velocity=7500 $mL.g^{-1}.h^{-1}$.

Operando XAS investigation of Mo/TiO_2 catalysts

AHM decomposition on TiO_2 vs. Mo/TiO_2 reduction investigated by Quick XANES

Figure 4 reports the results of *in situ* XAS monitoring of ammonium heptamolybdate (AHM) decomposition (amount corresponding to 3 wt% Mo loading) over the three TiO_2 supports when linearly heating them up to *ca*. 800 °C under hydrogen flow (the Mo/TiO_2 catalysts in Table 1 were prepared from a similar treatment, though with a maximum temperature of 500 °C). In all cases, in the course of the reductive treatment, the pre-edge feature disappears, and the edge shifts to lower energy. This corresponds to reduction of supported polymolybdates with distorted octahedral structure[39] during AHM decomposition under hydrogen. A rough comparison with the references (Figure 2b) suggests a transition from a MoO_3-like (Mo^{VI}) to a MoO_2-like (Mo^{IV}) state. However, while the initial states are relatively similar for the three AHM/TiO_2 samples, the final state of AHM/RNR is different from those of AHM/DT51D and AHM/P25 (*vide infra*).

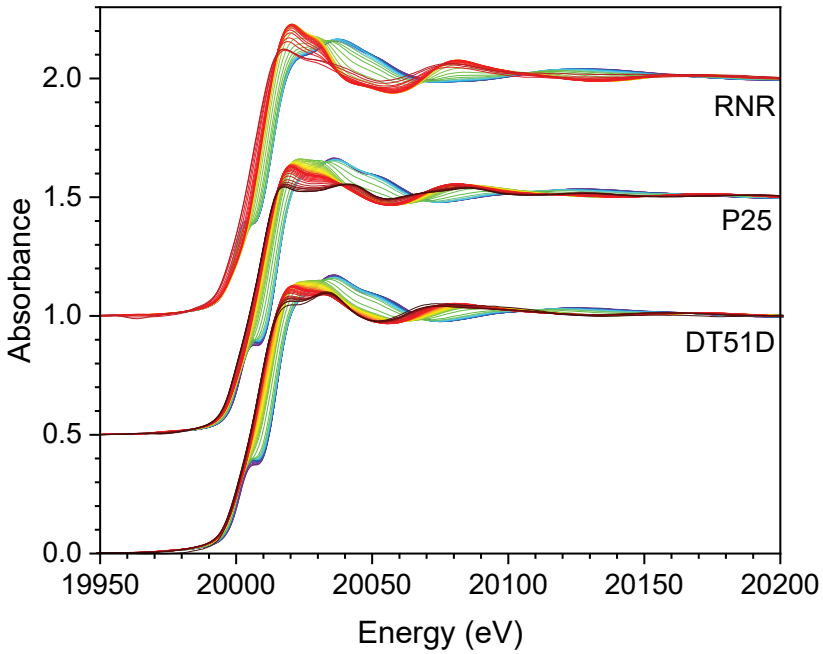

Figure 4. X-ray absorption spectra at the Mo K edge recorded during the decomposition of AHM on TiO_2 in H_2 flow (1 atm, 30 mL/min) from RT (purple-blue color) to ca. 800 °C (red-brown color). The target Mo loading was 3 wt% for all samples. P25 and RNR spectral series have been shifted vertically for ease of reading.

Principal component analysis (PCA) shows (Figure S14) that the three series of spectra can be decomposed in four pure components through MCR-ALS analysis, as reported in Figure 5. By comparison with the references of Figure 2b, it is possible to infer the oxidation state of Mo species in each component. The first component is the initial supported molybdate, with an oxidation degree of VI. For anatase-rich samples (DT51D and P25), the second component begins to form at *ca*. 200 °C and may correspond to a Mo^{V} species, while the third component is a MoO_2-like Mo^{IV} species forming at *ca*. 300 °C, and the fourth component formed above *ca*. 400 °C would roughly correspond to Mo^{III} species. For rutile nanorods, there is a downshift in the reduction temperatures, *i.e.* the second component is more quickly converted around 300 °C into the third component. The latter is quasi identical to the XANES spectrum of the 3Mo/RNR catalyst reduced *in situ* at 450 °C (see below). The third component is also more reducible on RNR than on P25 and D51D and already at 590 °C is totally converted into component 4 (Figure 5). The fourth component is not metallic but a strongly reduced Mo species that still has a majority of oxygen neighbors.

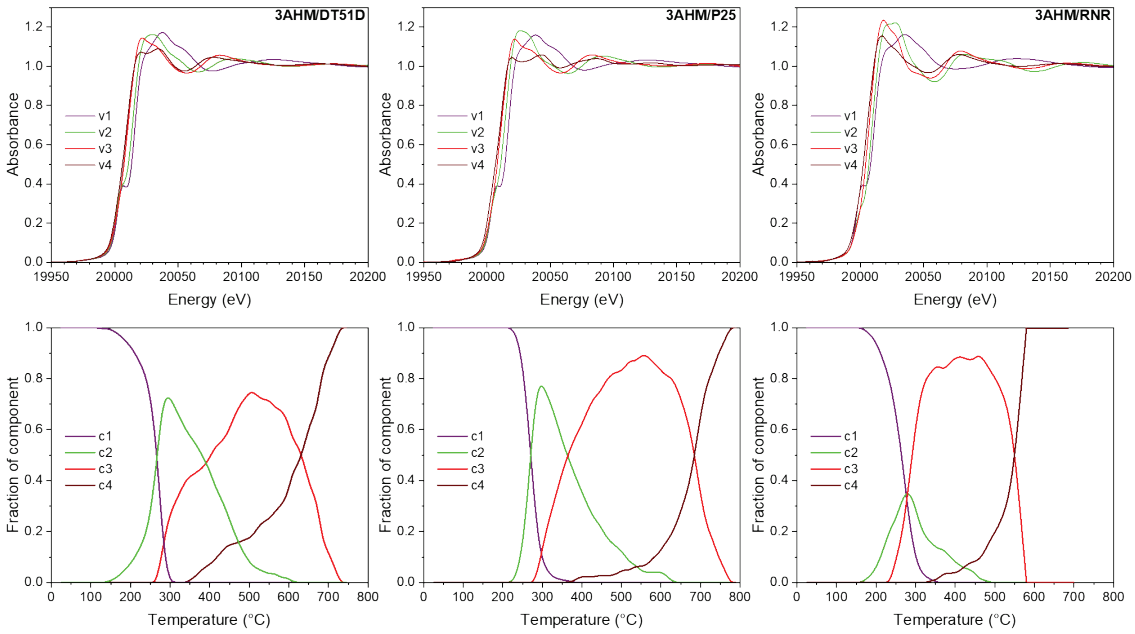

Figure 5. MCR-ALS decomposition of X-ray absorption spectra series corresponding to reductive treatments of AHM/TiO_2 impregnates (RT-800 °C). The target Mo loading was 3 wt% in all cases.

In a second series of experiments, similarly to laboratory catalytic tests, fresh 3 wt% and 10 wt% Mo/TiO_2 catalysts were treated in H_2 flow at atmospheric pressure up to 450 °C, then exposed to an H_2:CO_2 (3:1) reactant mixture at a total pressure of 2 MPa and heated up to 350 °C. Figure S15 shows

an example of experiments from the viewpoint of mass spectrometry monitoring. The XANES and EXAFS data (Fourier transform, FT, and continuous Cauchy wavelet transform, CCWT) for 3 wt% Mo reported in Figure 6 were recorded at quasi steady state: i) in static air at RT, then ii) at the end of the reduction step (H_2 flow, 1 atm, 450 °C), then iii) at the end of the reaction step (H_2+CO_2 flow, 2 MPa, 350 °C) or afterwards (1 atm, ~60 °C). No significant difference in XAS signal was observed between the reaction temperatures (from 275 to 350 °C), neither between reaction conditions and low-P low-T post-reaction ones. Figures S11, S12 and S16 provide additional EXAFS data ($\chi(k)$, FT imaginary part and CCWT before reduction), and the best fitting parameters are collected in Table S1. Table 2 gathers the main results for 3 wt% Mo/TiO_2 catalysts under H_2 treatment at 450 °C.

Table 2. EXAFS fitting values for 3 wt% Mo/TiO_2 catalysts under H_2 flow at 450 °C.

Scatterer	Coordination number	Radial distance (Å)
	3Mo/DT51D	
O	0.9(3)	1.72(2)
O	2.4(5)	2.05(2)
	3Mo/P25	
O	4.3(5)	2.07(2)
Mo	2.9(5)	2.76(2)
	3Mo/RNR	
O	3.0(5)	1.99(3)
O	2.0(3)	2.08(2)
Mo	1.1(2)	2.56(3)
O	3.9(7)	3.34(2)

Values in parentheses represent the uncertainty on the last significant digit.

The initial Mo state corresponds to fresh catalysts in air, i.e. previously prepared by AHM impregnation over titania and H_2 treatment at up to 500 °C at the laboratory. Figure 6 (top row) shows that, compared to the initial states of the impregnates in Figure 4, the pre-edge contribution in the spectra of the three as-prepared catalysts is less pronounced but still significant. This feature disappears upon the reducing treatment of Mo/TiO_2, similarly to the case of AHM reductive decomposition. The main modifications in XAS spectra occur during this reduction step, whereas the reaction conditions induce low to negligible change when going from anatase (DT51D) to rutile (RNR).

Figure S17 shows that, for all three supports, fresh and reduced states are similar to the intermediate states observed at *ca*. 270 °C and *ca*. 370 °C, respectively, in the corresponding AHM/TiO_2 reduction series (Figure 4). This indicates that Mo in the as-prepared (i.e. pre-reduced) catalysts was significantly oxidized in ambient air prior to the XAS experiments, which led to an *in situ* re-reduction sequence resembling that of AHM decomposition. However, for Mo/RNR, a higher temperature is needed *(ca*.

300 °C) for AHM reduction to reach the fresh catalyst state. This indicates that this catalyst may be more stable in air and better retain its reduced state, as previously shown by the comparison with other oxides (Figure 2).

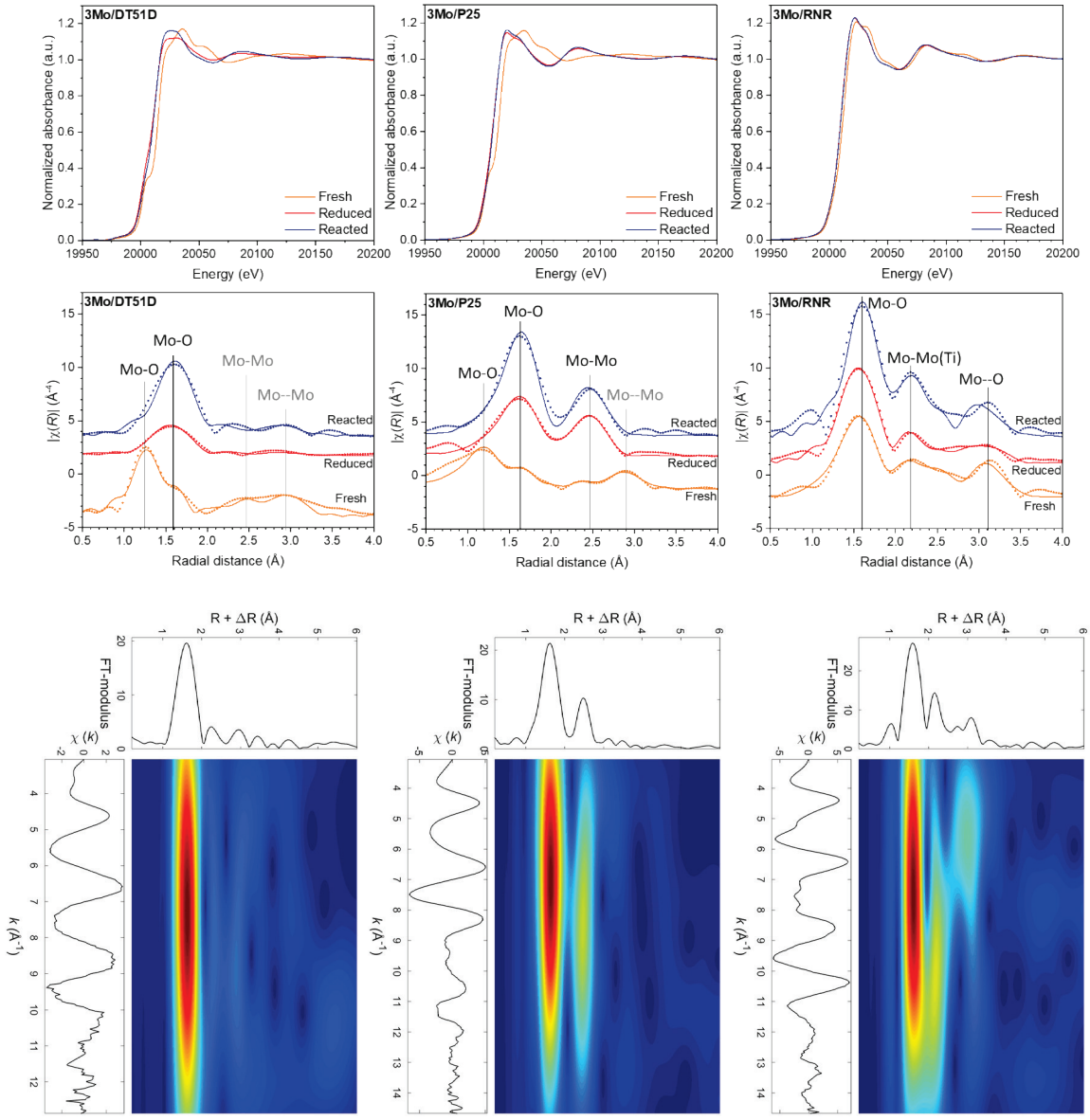

Figure 6. XANES absorbance (1st row), EXAFS Fourier transform modulus (2nd row) and post-reaction EXAFS continuous Cauchy wavelet transform modulus (3rd row). The thin lines in EXAFS FT data correspond to best numerical fits. Radial distances are not phase-corrected. EXAFTS FT data have been shifted vertically for ease of reading. Assignments of EXAFS FT peaks are indicated in black (strong signal) or grey (weak signal). "Fresh", "reduced" and "reacted" states correspond to recording conditions (air, RT, 1 atm), (H_2, 450 °C, 1 atm) and (H_2+CO_2, 350 °C, 2 MPa), respectively.

PCA shows that the three series of spectra corresponding to the reduction of Mo/TiO_2 catalysts can be decomposed in three pure components through MCR-ALS analysis (Figure S18 shows an example for P25), like the AHM/TiO_2 impregnates in the same RT-450 °C temperature range, although the impregnates required one or two additional components at higher temperature (Figure 5). Moreover, the evolutions of the first three component concentrations during AHM/TiO_2 decomposition-reduction are similar to those for Mo/TiO_2 reduction.

Structural differences between Mo/TiO_2 catalysts investigated by EXAFS

The EXAFS FT data in Figure 6 (middle row) point out important differences between the three catalysts, at each step. Overall, letting aside the initial state, only light short-distance neighbors can be seen for Mo/DT51D, which are supplemented by a heavy medium-distance neighbor for Mo/P25, itself supplemented by a light long-distance neighbor for Mo/RNR. This is confirmed by the CCWT analysis of Figure 6 (bottom row), which shows that the spot for this long-distance neighbor is located at low *k*, between 5 and 6 $Å^{-1}$ (compare with the spot of the second (Mo) neighbor, centered at *k* between 9 and 10 $Å^{-1}$).

Let us analyze the results from the EXAFS data and the direct comparison of absorbance spectra in Figure S19. In the latter, the jump energy at 0.5 absorbance provides an estimate of the Mo oxidation state.[40,41] For Mo supported on anatase (DT51D), the fresh state corresponds to highly disordered MoO_3-type oxide with distorted octahedral environment, *i.e.* adsorbed polyoxomolybdate species.[39] The final ("reacted") state corresponds to partially reduced Mo oxide, with Mo possibly in the oxidation state IV in the form of MoO_2 single atoms or few-atom clusters. While only (four) Mo-O bonds of 2.07 Å in length are detected in 3Mo/DT51D, three long Mo-O-Mo scattering paths (2.75 Å) are additionally visible in 10Mo/DT51D (Table S1), confirming the Mo coverage effect on Mo dispersion suggested by STEM.

It is interesting to compare our XAS results to those of Tougerti and coworkers, who submitted their 7.5 wt% MoO_3/TiO_2 (anatase) catalyst to a similar reducing treatment (10% H_2/N_2 flow, 400 °C).[42] Figure S20 shows similarities between both sets of data, allowing us to infer that Mo species on anatase TiO_2 are in the form of oxomolybdate single atoms and flat (monolayer) clusters that undergo Mo^{VI} to Mo^{V} reduction, as previously observed using NAP-XPS.[25] Moreover, this is consistent with our MCR-ALS analysis showing that at 400 °C (and under 1 atm H_2 flow), Mo^{V} species are incompletely converted into Mo^{IV} species (Figure 5 and Figure S18). This work also suggests that only monoxo Mo=O bonds would be reduced, while dioxo would not.[42]

In contrast, RNRs enable faster and further reduction, at least to Mo^{IV} (Figure 5 and Figure S19), which is also consistent with NAP-XPS experiments.[25] Up to *R*=2.5 Å, the EXAFS FT and CCWT patterns are similar for Mo/RNR in the final state and the (rutile) MoO_2 reference (see the direct comparison in Figure S21), and the fitting indicates that Mo has five O nearest-neighbors, instead of six for MoO_2 (Table S1). This result is still valid for 10Mo/RNR, which also exhibits – like 3Mo/RNR – about one Mo-Mo bond of length 2.55 Å. As discussed below, this heavy neighbor coordination sphere may also contain Ti atoms.

Regarding the case of Mo/P25, while initially the EXAFS signal for 3Mo/P25 is close to that for 3Mo/DT51D, in the reduced and reacted states a clear Mo neighbor (*CN*=2.9, *R*=2.76 Å) is present only for P25. The data suggest that initial Mo-O-Mo moieties (*CN*=1.0 and *R*=3.29 Å for Mo neighbor) are converted into Mo-Mo ones upon reduction. The difference from the DT51D structure may originate from the lower surface area and/or the anatase-rutile phase mixture for P25 (Table 1).

The EXAFS results showing the relative similarity in Mo coordination between Mo/RNR and bulk MoO_2 suggest that Mo cations may replace Ti cations, at least in the near-surface region of rutile titania, and are consistent with the similar structures of rutile TiO_2 and MoO_2. High-resolution STEM images in the present work and in our previous one [25] indicate that Mo on rutile is more dispersed in the form of single atoms than on anatase, onto which clusters are more present. STEM and other investigations also suggest that Mo cations can locate above Ti positions or replace Ti cations at the surface of both rutile and anatase TiO_2.[25,39,43,44]

Discussion

EXAFS fitting of multiple shells

A simple visual comparison of the EXAFS FT moduli of the 3Mo/TiO_2 samples (Figure S11) suggests that both the number of Mo coordination shells and their parameters, such as *CN* and *R*, strongly vary from one sample to another, which is confirmed by the fitting results (Table S1). The multitude of shells in some samples and their complex evolution originate from the sample preparation and the nature of the corresponding species, which are often present as mixtures and depend on the oxide support, the Mo loading and the treatment conditions.

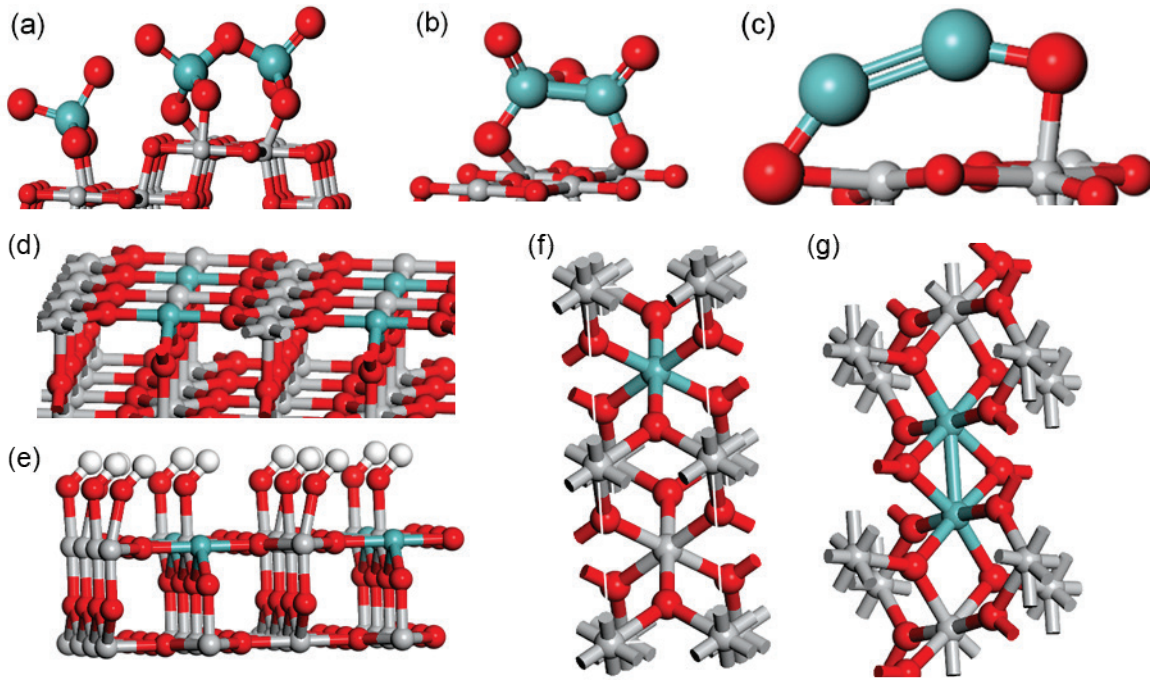

Figure 7. DFT models of Mo atoms interacting with the rutile TiO_2(110) surface, showing possible Mo coordinations and explaining the multiplicity and versatility of shells in the EXAFS fitting. a-c) surface grafted (Mo is gradually reduced from Mo^{IV} to Mo^{II} from left to right). d-e) surface-substituted, without or with hydroxyls; f-g) bulk-substituted with Mo monomer or dimer.

As known from the literature (see e.g. Ref. 39), as-prepared air-calcined MoO_x/TiO_2 solids – that we did not study here – contain monomers and oligomers of Mo^{VI} molybdates (see FDMNES structural model in Figure 7a). However, our starting samples for the XAS experiments were already pre-reduced with hydrogen at 500 °C, then partially re-oxidized due to exposure to ambient air. In these samples, several oxidation states of Mo might be present, namely Mo^{VI}, Mo^{V}, and Mo^{IV}, which explains the presence of different shells in EXAFS. The Mo^{VI} species contribute with a short double Mo=O bond (R ≈ 1.7 Å) as in MoO_3, as well as with long Mo-O bonds (R > 1.9 Å), typical for Mo-O-Mo and Mo-O-Ti fragments (R > 3 Å), as in supported Mo^{VI} oligomolybdate species (Figure 7a). Since in the EXAFS of bulk MoO_2 five shells were reliably fitted (Table S1), the corresponding shells can be present in samples that contain MoO_2 nanoparticles (fresh 10Mo/P25). Therefore, the number of shells could easily go beyond four, which makes the fitting task challenging. Moreover, the Mo species have a range of Mo-O distances as they are strongly distorted. With this respect, the fitting results represent only the main features and the average values. Thus, for example, the long-distance Mo-O shells (R ≈ 1.9 to 2.0 Å) existing in both Mo^{VI} and Mo^{IV} species could not be possibly resolved and should be represented by a common average shell. In most cases, four shells or less were sufficient to fit the spectra: short Mo=O, long Mo-O, metallic Mo-Mo and non-bonded Mo-O-Mo shells. However, a greater number of shells,

up to six, was necessary to adequately represent the spectra when Mo^{VI} species with short Mo=O distances and long non-bonded Mo-O-Mo ones coexist with MoO_2 particles and/or a solid solution (see *ex situ* samples 10Mo/P25 and 3Mo/RNR in Table S1).

After *in situ* reduction and/or after exposure to the reaction mixture ("reduced" and "reacted" samples in Table S1), the Mo=O ($R \approx 1.7$ Å) and Mo-O-Mo ($R > 3$ Å) moieties decrease or completely disappear, whereas the number of metallic Mo-Mo bonds ($R \approx 2.5$ Å) increase, as the Mo-O-Mo fragments are transformed into Mo-Mo ones (Figure 7b,c).

Formation of a solid solution by substitution of Ti^{IV} with Mo^{IV} in the rutile surface or subsurface layer (Figure 7d-g) would result in a more ordered coordination environment, bearing considerable similarity with the MoO_2 structure.

Surface and subsurface Mo doping

The difference between anatase and rutile titania supports may arise from the different adsorption strengths as well as the different solubilities of Mo^{IV} species in these phases. In the latter hypothesis, for anatase, molybdenum would remain on the surface and its coordination is thus different from that in rutile lattice. Moreover, on anatase the reduction-to-reaction environment switch leads to more significant variation of the mean coordination parameters than for rutile (Figure 6 and Table S1), which contains always the same majority species. Similarly, the increase in Mo coverage has much more influence on the Mo/DT51D structure (Figure S20) than on the Mo/RNR one (Figure S21). For a random substitution of Ti atoms with Mo atoms in the rutile titania lattice to form a solid solution,[45–47] Ti atoms should be predominant in the second coordination shell of molybdenum (as Mo-Ti moieties). However, from EXAFS it is difficult to discriminate Mo-Mo and Mo-Ti neighbors, which could be present simultaneously and at similar distances. Indeed, Mo^{IV} dissolution in the rutile structure leads to significant Mo clustering along the *c* axis, with the formation of Mo-Mo bonds.[45]

In order to tentatively determine the nature of Mo species, the XANES spectra of Mo/RNR catalysts were confronted with FDMNES simulations. The structural models in Figure 7 are complemented with those in Figures S22-S23, while the corresponding simulated XANES spectra are reported in Figure S24, and comparisons with experiments are shown in Figure S25. Table S2 provides the CNs and the bond lengths associated to the models.

For surface-grafted structures (Figure 7a -c and Figure S24a), the variations of simulated XANES are the strongest, like the corresponding changes in Mo coordination. The spectrum of grafted Mo^{VI} species expectedly contains a very strong pre-edge feature which decreases upon reduction to Mo^{IV}. The

spectra of Mo^{VI} and Mo^{II} surface-grafted species are very dissimilar to the recorded spectra, whereas that of Mo^{IV} is more similar, though it still contains a pre-edge, not observed in the "reduced" and "reacted" samples. For the bulk-substituted structures (Figure 7f, Figure S22 and Figure S24b), the spectra show the expected shift toward lower energy from Mo^{IV} to Mo^{II}, by about 1.5 eV per oxidation state. For the surface-substituted structures (Figure 7d-e, Figure S23 and Figure S24c), one observes an expected shift of edge jump to lower energy by 2.5-3.0 eV, from the spectra of Mo^{VI} species containing a Mo=O group to the structures containing bare Mo^{IV} atoms. The overall two-lobe shape of XANES remains similar whatever the surface-substituted structure and not far from the bulk-substituted ones, with peaks at relative energies of 16-18 and 31-33 eV.

All substituted structures reproduce the two-lobe shape of XANES spectra (Figure S25). The surface-substituted structures reproduce relatively well the shape and the energy of features of experimental spectra, though the second feature is exaggerated in the models and shifted to the right. The simulated spectrum of MoO_2 diverges in the first peak but otherwise reproduces better the overall shape. Finally, the bulk-substituted dimer structure better reproduces the positions and relative intensities of the first two peaks. However, none of the simulated spectra perfectly reproduces the experimental spectra, as can be expected in the presence of several complex species.

In a final attempt to identify a possible MoO_2-TiO_2 solid solution where Mo would replace Ti in the rutile TiO_2 lattice, 3Mo/RNR and 3Mo/DT51D were analyzed *in situ* by X-ray diffraction while being heated from RT to 700 °C in H_2 flow. The detailed investigation is reported as Supporting Information, Figures S26-S28 and Discussion. The evolutions of the lattice parameters are consistent with a partial dissolution of Mo atoms in the titania lattice. Given the catalyst preparation method employed (impregnation) and the significant catalytic activities, doping is likely to concern only the near-surface region of titania. Since XAS indicates the presence of MoO_x clusters on anatase, Mo doping is less extended for this support.

Overall, the structural results (STEM, XAS, XRD) concord with a stronger tendency to single-atomic Mo dispersion on rutile (110) facets and a partial Ti-Mo substitution in the near-surface region of the RNRs. It also turns out that Mo/TiO_2 is a complex system with several co-existing species that all contribute to the XAS signal. In this regard, while our *operando* data suggest that Mo/RNR is more ordered (long Mo-O bonds) and poorly sensitive to the thermochemical environment, the contribution of reduced polymolybdates[42] in epitaxy on the (110) surface facets of the nanorods, similar to the flat Mo oxide clusters seen on anatase and expected to exhibit a MoO_2-like environment, cannot be ruled out. Besides, in order to understand the CO_2 hydrogenation performances of Mo/TiO_2 catalysts, not only

the nature of Mo species but also the influence of the titania surface structure on *e.g.* CO_2 chemisorption and activation will have to be considered in the future.

Conclusion

Catalysts consisting of molybdenum atomically dispersed – as evidenced from STEM and XAS – on a variety of transition metal oxides, have been compared for CO_2 hydrogenation under high-pressure flow conditions. The most efficient systems in terms of CO_2 conversion activity are titania-supported catalysts, among which molybdenum supported on rutile nanorods (RNRs) is the most active and the most selective to methanol. The preparation of Mo/TiO_2 (RNR, DT51D anatase, and P25) catalysts and their structural evolution upon reduction pretreatment and catalytic testing have been investigated by *operando* Quick XANES and EXAFS. In terms of Mo state, the reductive decomposition of adsorbed polymolybdates resembles the reduction of as-prepared catalysts. As shown by MCR-ALS computational treatment, the average Mo oxidation state switches from VI to V at 200-300 °C, then from V to IV at 300-500 °C. Further heating leads to full reduction of molybdenum.

However, the rutile-supported catalyst exhibits a distinct behavior, with the fastest formation of reduced Mo^{IV} species. The average *operando* oxidation state of Mo on rutile is slightly lower than on anatase. For Mo/RNR, the structural change induced by reaction conditions ($3H_2 + CO_2$, 2 MPa) with respect to reduction conditions (H_2, 1 atm) is minor, and the partially reduced Mo species are identified as the catalytically active ones. EXAFS indicates that Mo is coordinated to much fewer atoms on anatase (4 first-neighbor O for 3Mo/DT51D) as compared to rutile (5 first-neighbor O, 1 first-neighbor Mo, 5 second-neighbor O for 3Mo/RNR) under the same reduction or reaction conditions. Together with the stronger effect of the Mo coverage and the reaction conditions on anatase, this conducts us to propose that Mo species on anatase consist of surface-adsorbed Mo clusters and single atoms, whereas a significant fraction of surface Ti atoms are substituted with Mo atoms on rutile. The latter configuration, also supported by *in situ* XRD, appears to maximize the CO_2 hydrogenation activity and the selectivity to methanol.

These findings may inspire further improvements of the Mo/TiO_2 system and related eco-efficient oxide materials based on early transition metals for CO_2 valorization.

Supporting Information

Supplementary XANES/EXAFS data and analyses, modeling and simulations of XANES spectra, mass spectrometry data, supplementary TEM/STEM/EDX data, supplementary catalysis data for Mo/ZnO, *ex situ* XRD data, *in situ* XRD data and corresponding discussion.

Acknowledgement

L. Barthe & S. Belin (SOLEIL: XAS), Y. Lefkir (LabHC: STEM-HAADF), F. Bosselet & Y. Ayzac (IRCELYON: XRD), N. Bonnet & P. Mascunan (IRCELYON: ICP-OES, XRF), J.M. Panadés-Blas & L. Muller (IRCELYON: non-titania sample preparation) are thanked for their contributions to this work.

Agence Nationale de la Recherche (UltraCat project, ANR-17-CE06-0008) is acknowledged for financial support. SOLEIL synchrotron and ROCK beamline (supported by ANR-10-EQPX45 program) are acknowledged for access to XAS apparatus. CLYM is acknowledged for access to Titan and NeoARM microscopes.

References

(1) Zhong, J.; Yang, X.; Wu, Z.; Liang, B.; Huang, Y.; Zhang, T. State of the Art and Perspectives in Heterogeneous Catalysis of CO2 Hydrogenation to Methanol. *Chem. Soc. Rev.* **2020**, *49* (5), 1385–1413. https://doi.org/10.1039/C9CS00614A.

(2) Golunski, S.; Burch, R. CO2 Hydrogenation to Methanol over Copper Catalysts: Learning from Syngas Conversion. *Top. Catal.* **2021**, *64* (17), 974–983. https://doi.org/10.1007/s11244-021-01427-y.

(3) *Element Scarcity - EuChemS Periodic Table*. EuChemS. https://www.euchems.eu/euchems-periodic-table/ (accessed 2023-06-20).

(4) *Final List of Critical Minerals 2022 – Policies*. IEA. https://www.iea.org/policies/15271-final-list-of-critical-minerals-2022 (accessed 2023-06-20).

(5) Fujitani, T.; Saito, M.; Kanai, Y.; Watanabe, T.; Nakamura, J.; Uchijima, T. Development of an Active Ga2O3 Supported Palladium Catalyst for the Synthesis of Methanol from Carbon Dioxide and Hydrogen. *Appl. Catal. Gen.* **1995**, *125* (2), L199–L202. https://doi.org/10.1016/0926-860X(95)00049-6.

(6) Martin, O.; Martín, A. J.; Mondelli, C.; Mitchell, S.; Segawa, T. F.; Hauert, R.; Drouilly, C.; Curulla-Ferré, D.; Pérez-Ramírez, J. Indium Oxide as a Superior Catalyst for Methanol Synthesis by CO2 Hydrogenation. *Angew. Chem. Int. Ed.* **2016**, *55* (21), 6261–6265. https://doi.org/10.1002/anie.201600943.

(7) Dong, X.; Li, F.; Zhao, N.; Xiao, F.; Wang, J.; Tan, Y. CO2 Hydrogenation to Methanol over Cu/ZnO/ZrO2 Catalysts Prepared by Precipitation-Reduction Method. *Appl. Catal. B Environ.* **2016**, *191*, 8–17. https://doi.org/10.1016/j.apcatb.2016.03.014.

(8) Chen, S.; Abdel-Mageed, A. M.; Mochizuki, C.; Ishida, T.; Murayama, T.; Rabeah, J.; Parlinska-Wojtan, M.; Brückner, A.; Behm, R. J. Controlling the O-Vacancy Formation and Performance of Au/ZnO Catalysts in CO2 Reduction to Methanol by the ZnO Particle Size. *ACS Catal.* **2021**, *11* (15), 9022–9033. https://doi.org/10.1021/acscatal.1c01415.

(9) Hu, J.; Yu, L.; Deng, J.; Wang, Y.; Cheng, K.; Ma, C.; Zhang, Q.; Wen, W.; Yu, S.; Pan, Y.; Yang, J.; Ma, H.; Qi, F.; Wang, Y.; Zheng, Y.; Chen, M.; Huang, R.; Zhang, S.; Zhao, Z.; Mao, J.; Meng, X.; Ji, Q.; Hou, G.; Han, X.; Bao, X.; Wang, Y.; Deng, D. Sulfur Vacancy-Rich MoS2 as a Catalyst for the Hydrogenation of CO2 to Methanol. *Nat. Catal.* **2021**, *4* (3), 242–250. https://doi.org/10.1038/s41929-021-00584-3.

(10) Posada-Pérez, S.; Ramírez, P. J.; Evans, J.; Viñes, F.; Liu, P.; Illas, F.; Rodriguez, J. A. Highly Active Au/δ-MoC and Cu/δ-MoC Catalysts for the Conversion of CO_2 : The Metal/C Ratio as a Key Factor Defining Activity, Selectivity, and Stability. *J. Am. Chem. Soc.* **2016**, *138* (26), 8269–8278. https://doi.org/10.1021/jacs.6b04529.

(11) Lang, R.; Du, X.; Huang, Y.; Jiang, X.; Zhang, Q.; Guo, Y.; Liu, K.; Qiao, B.; Wang, A.; Zhang, T. Single-Atom Catalysts Based on the Metal–Oxide Interaction. *Chem. Rev.* **2020**, *120* (21), 11986–12043. https://doi.org/10.1021/acs.chemrev.0c00797.

(12) Piccolo, L. Restructuring Effects of the Chemical Environment in Metal Nanocatalysis and Single-Atom Catalysis. *Catal. Today* **2021**, *373*, 80–97. https://doi.org/10.1016/j.cattod.2020.03.052.

(13) *Supported Metal Single Atom Catalysis*, P. Serp&D. Pham Minh (Eds.).; Wiley-VCH: Weinheim, 2022. https://doi.org/10.1002/9783527830169.

(14) Liu, L.; Li, M.; Chen, F.; Huang, H. Recent Advances on Single-Atom Catalysts for CO2 Reduction. *Small Struct.* **2023**, *4* (3), 2200188. https://doi.org/10.1002/sstr.202200188.

(15) Ye, J.; Liu, C.; Mei, D.; Ge, Q. Active Oxygen Vacancy Site for Methanol Synthesis from CO2 Hydrogenation on In2O3(110): A DFT Study. *ACS Catal.* **2013**, *3* (6), 1296–1306. https://doi.org/10.1021/cs400132a.

(16) Cao, A.; Wang, Z.; Li, H.; Nørskov, J. K. Relations between Surface Oxygen Vacancies and Activity of Methanol Formation from CO2 Hydrogenation over In2O3 Surfaces. *ACS Catal.* **2021**, *11* (3), 1780–1786. https://doi.org/10.1021/acscatal.0c05046.

(17) Frei, M. S.; Mondelli, C.; García-Muelas, R.; Kley, K. S.; Puértolas, B.; López, N.; Safonova, O. V.; Stewart, J. A.; Ferré, D. C.; Pérez-Ramírez, J. Atomic - Scale Engineering of Indium Oxide Promotion by Palladium for Methanol Production via CO 2 Hydrogenation. *Nat. Commun.* **2019**, *10* (1), 1–11. https://doi.org/10.1038/s41467-019-11349-9.

(18) Dostagir, N. H. M.; Thompson, C.; Kobayashi, H.; Karim, A. M.; Fukuoka, A.; Shrotri, A. Rh Promoted In2O3 as a Highly Active Catalyst for CO2 Hydrogenation to Methanol. *Catal. Sci. Technol.* **2020**, *10* (24), 8196–8202. https://doi.org/10.1039/D0CY01789B.

(19) Toyao, T.; Kayamori, S.; Maeno, Z.; Siddiki, S. M. A. H.; Shimizu, K. Heterogeneous Pt and MoOx Co-Loaded TiO_2 Catalysts for Low-Temperature CO_2 Hydrogenation To Form CH_3OH. *ACS Catal.* **2019**, *9* (9), 8187–8196. https://doi.org/10.1021/acscatal.9b01225.

(20) Ting, K. W.; Toyao, T.; Siddiki, S. M. A. H.; Shimizu, K. Low-Temperature Hydrogenation of CO2 to Methanol over Heterogeneous TiO2-Supported Re Catalysts. *ACS Catal.* **2019**, *9* (4), 3685–3693. https://doi.org/10.1021/acscatal.8b04821.

(21) Kuwahara, Y.; Mihogi, T.; Hamahara, K.; Kusu, K.; Kobayashi, H.; Yamashita, H. A Quasi-Stable Molybdenum Sub-Oxide with Abundant Oxygen Vacancies That Promotes CO2 Hydrogenation to Methanol. *Chem. Sci.* **2021**, *12* (29), 9902–9915. https://doi.org/10.1039/D1SC02550C.

(22) Cao, F.; Gong, N.; Ma, Z.; Wang, X.; Tan, M.; Wu, Y.; Tan, Y. Controlling CO2 Hydrogenation Selectivity by Rh-Based Catalysts with Different Crystalline Phases of TiO2. *Chem. Commun.* **2022**, *58*, 4219–4222. https://doi.org/10.1039/D2CC00472K.

(23) Iyemperumal, S. K.; Pham, T. D.; Bauer, J.; Deskins, N. A. Quantifying Support Interactions and Reactivity Trends of Single Metal Atom Catalysts over TiO2. *J. Phys. Chem. C* **2018**, *122* (44), 25274–25289. https://doi.org/10.1021/acs.jpcc.8b05611.

(24) Zhou, J.; Gao, Z.; Xiang, G.; Zhai, T.; Liu, Z.; Zhao, W.; Liang, X.; Wang, L. Interfacial Compatibility Critically Controls Ru/TiO2 Metal-Support Interaction Modes in CO2 Hydrogenation. *Nat. Commun.* **2022**, *13* (1), 327. https://doi.org/10.1038/s41467-021-27910-4.

(25) Len, T.; Bahri, M.; Ersen, O.; Lefkir, Y.; Cardenas, L.; Villar-Garcia, I. J.; Dieste, V. P.; Llorca, J.; Perret, N.; Checa, R.; Puzenat, E.; Afanasiev, P.; Morfin, F.; Piccolo, L. Ultradispersed Mo/TiO2

Catalysts for CO2 Hydrogenation to Methanol. *Green Chem.* **2021**, *23* (18), 7259–7268. https://doi.org/10.1039/D1GC01761F.
(26) Barrault, J.; Urresta, J. Hydrogénation du dioxyde de carbone en méthanol en présence de catalyseurs à base de molybdène. *Comptes Rendus Académie Sci. - Ser. IIC - Chem.* **1999**, *2* (3), 167–174. https://doi.org/10.1016/S1387-1609(99)80060-7.
(27) Li, H.; Afanasiev, P. On the Selective Growth of Titania Polymorphs in Acidic Aqueous Medium. *Mater. Res. Bull.* **2011**, *46* (12), 2506–2514. https://doi.org/10.1016/j.materresbull.2011.08.023.
(28) Li, H.; Vrinat, M.; Berhault, G.; Li, D.; Nie, H.; Afanasiev, P. Hydrothermal Synthesis and Acidity Characterization of TiO2 Polymorphs. *Mater. Res. Bull.* **2013**, *48* (9), 3374–3382. https://doi.org/10.1016/j.materresbull.2013.05.017.
(29) Konuspayeva, Z.; Afanasiev, P.; Nguyen, T.-S.; Di Felice, L.; Morfin, F.; Nguyen, N.-T.; Nelayah, J.; Ricolleau, C.; Li, Z. Y.; Yuan, J.; Berhault, G.; Piccolo, L. Au–Rh and Au–Pd Nanocatalysts Supported on Rutile Titania Nanorods: Structure and Chemical Stability. *Phys. Chem. Chem. Phys.* **2015**, *17* (42), 28112–28120. https://doi.org/10.1039/C5CP00249D.
(30) Briois, V.; Fontaine, C. L.; Belin, S.; Barthe, L.; Moreno, T.; Pinty, V.; Carcy, A.; Girardot, R.; Fonda, E. ROCK: The New Quick-EXAFS Beamline at SOLEIL. *J. Phys. Conf. Ser.* **2016**, *712*, 012149. https://doi.org/10.1088/1742-6596/712/1/012149.
(31) Ankudinov, A. L.; Ravel, B.; Rehr, J. J.; Conradson, S. D. Real-Space Multiple-Scattering Calculation and Interpretation of x-Ray-Absorption near-Edge Structure. *Phys. Rev. B* **1998**, *58* (12), 7565–7576. https://doi.org/10.1103/PhysRevB.58.7565.
(32) Klementev, K. V. Extraction of the Fine Structure from X-Ray Absorption Spectra. *J. Phys. Appl. Phys.* **2001**, *34* (2), 209. https://doi.org/10.1088/0022-3727/34/2/309.
(33) Genuit, D.; Afanasiev, P.; Vrinat, M. Solution Syntheses of Unsupported Co(Ni)–Mo–S Hydrotreating Catalysts. *J. Catal.* **2005**, *235* (2), 302–317. https://doi.org/10.1016/j.jcat.2005.08.016.
(34) Muñoz, M.; Farges, F.; Argoul, P. Continuous Cauchy Wavelet Transform of XAFS Spectra. *Phys. Scr.* **2005**, *2005* (T115), 221. https://doi.org/10.1238/Physica.Topical.115a00221.
(35) Rochet, A.; Baubet, B.; Moizan, V.; Pichon, C.; Briois, V. Co-K and Mo-K Edges Quick-XAS Study of the Sulphidation Properties of Mo/Al2O3 and CoMo/Al2O3 Catalysts. *Comptes Rendus Chim.* **2016**, *19* (10), 1337–1351. https://doi.org/10.1016/j.crci.2016.01.009.
(36) Jaumot, J.; de Juan, A.; Tauler, R. MCR-ALS GUI 2.0: New Features and Applications. *Chemom. Intell. Lab. Syst.* **2015**, *140*, 1–12. https://doi.org/10.1016/j.chemolab.2014.10.003.
(37) Bunău, O.; Joly, Y. Self-Consistent Aspects of x-Ray Absorption Calculations. *J. Phys. Condens. Matter* **2009**, *21* (34), 345501. https://doi.org/10.1088/0953-8984/21/34/345501.
(38) Farges, F.; Siewert, R.; Brown, G. E., Jr.; Guesdon, A.; Morin, G. STRUCTURAL ENVIRONMENTS AROUND MOLYBDENUM IN SILICATE GLASSES AND MELTS. I. INFLUENCE OF COMPOSITION AND OXYGEN FUGACITY ON THE LOCAL STRUCTURE OF MOLYBDENUM. *Can. Mineral.* **2006**, *44* (3), 731–753. https://doi.org/10.2113/gscanmin.44.3.731.
(39) Tougerti, A.; Berrier, E.; Mamede, A.-S.; La Fontaine, C.; Briois, V.; Joly, Y.; Payen, E.; Paul, J.-F.; Cristol, S. Synergy between XANES Spectroscopy and DFT to Elucidate the Amorphous Structure of Heterogeneous Catalysts: TiO2-Supported Molybdenum Oxide Catalysts. *Angew. Chem. Int. Ed.* **2013**, *52* (25), 6440–6444. https://doi.org/10.1002/anie.201300538.
(40) Ressler, T.; Timpe, O.; Neisius, T.; Find, J.; Mestl, G.; Dieterle, M.; Schlögl, R. Time-Resolved XAS Investigation of the Reduction/Oxidation of MoO3−x. *J. Catal.* **2000**, *191* (1), 75–85. https://doi.org/10.1006/jcat.1999.2772.
(41) Li, L.; Morrill, M. R.; Shou, H.; Barton, D. G.; Ferrari, D.; Davis, R. J.; Agrawal, P. K.; Jones, C. W.; Sholl, D. S. On the Relationship between Mo K-Edge Energies and DFT Computed Partial Charges. *J. Phys. Chem. C* **2013**, *117* (6), 2769–2773. https://doi.org/10.1021/jp309078a.
(42) Hu, H.; Oliveira de Souza, D.; Berrier, E.; Paul, J.-F.; La Fontaine, C.; Briois, V.; Cristol, S.; Tougerti, A. Investigation of the Reducibility of Supported Oxomolybdate Species for Mapping

of Active Centers of Partial Oxidation Reaction: In Situ Mo K-Edge XAS and DFT Study. *J. Phys. Chem. C* **2019**, *123* (30), 18325–18335. https://doi.org/10.1021/acs.jpcc.9b02732.
(43) Guo, S.; Huang, Z.; Wang, L.; Wu, X.; Shen, H.; Jing, G. MoO3/TiO2 Catalyst with Atomically Dispersed O-Mo-O Structures toward Improving NH4HSO4 Poisoning Resistance for Selective Catalytic Reduction of Nitrogen Oxides. *J. Hazard. Mater.* **2021**, *418*, 126289. https://doi.org/10.1016/j.jhazmat.2021.126289.
(44) Das, A.; Jones, L. O.; Chen, Y.; Choudhury, D.; Keane, D. T.; Elam, J. W.; Schatz, G. C.; Bedzyk, M. J. Atomic-Scale View of Redox Induced Changes for Monolayer MoOx on α-TiO2(110) with Chemical-State Sensitivity. *J. Phys. Chem. Lett.* **2022**, *13* (23), 5304–5309. https://doi.org/10.1021/acs.jpclett.2c01267.
(45) Valigi, M.; Gazzoli, D.; Jacono, M. L.; Minelli, G.; Porta, P. A Structural and Magnetic Study of the MoOx—TiO2 System. *Z. Für Phys. Chem.* **1982**, *132* (1), 29–40. https://doi.org/10.1524/zpch.1982.132.1.029.
(46) Cordischi, D.; Gazzoli, D.; Occhiuzzi, M.; Valigi, M. Redox Behavior of VI B Transition Metal Ions in Rutile TiO2 Solid Solutions: An XRD and EPR Study. *J. Solid State Chem.* **2000**, *152* (2), 412–420. https://doi.org/10.1006/jssc.2000.8698.
(47) Jacob, K. T.; Shekhar, C.; Waseda, Y. Thermodynamic Properties and Phase Diagram for the System MoO2–TiO2. *J. Am. Ceram. Soc.* **2008**, *91* (2), 563–568. https://doi.org/10.1111/j.1551-2916.2007.02165.x.